MethodsX 7 (2020) 100822

Contents lists available at ScienceDirect

MethodsX

journal homepage: www.elsevier.com/locate/mex

Method Article

High performance modeling of heterogeneous SOFC electrode microstructures using the MOOSE framework: ERMINE (Electrochemical Reactions in MIcrostructural NEtworks)

Tim Hsu[a,b], Rubayyat Mahbub[a,b], Jerry H. Mason[c,d], William K. Epting[a,c], Harry W. Abernathy[d,e], Gregory A. Hackett[d], Anthony D. Rollett[a,b], Shawn Litster[a,b,f], Paul A. Salvador[a,b,*]

[a] U.S. DOE National Energy Technology Laboratory, 626 Cochrans Mill Road, Pittsburgh, PA 15236, USA
[b] Department of Materials Science and Engineering, Carnegie Mellon University, 5000 Forbes Avenue, Pittsburgh, PA 15213, USA
[c] U.S. DOE National Energy Technology Laboratory, 3610 Collins Ferry Road, Morgantown, WV 26505, USA
[d] Leidos Research Support Team, 3610 Collins Ferry Road, Morgantown, WV 26505, USA
[e] Leidos Research Support Team, 626 Cochrans Mill Road, Pittsburgh, PA 15236, USA
[f] Department of Mechanical Engineering, Carnegie Mellon University, 5000 Forbes Avenue, Pittsburgh, PA 15213, USA

A B S T R A C T

Electrochemical energy devices, such as batteries and fuel cells, contain active electrode components that have highly porous, multiphase microstructures for improved performance. Predictive electrochemical models of solid oxide fuel cell (SOFC) electrode performance based on measured microstructures have been limited to small length scales, a small number of simulations, and/or relatively homogeneous microstructures. To overcome the difficulty in modeling electrochemical activity of inhomogeneous microstructures at considerable length scales, we have developed a high-throughput simulation application that operates on high-performance computing platforms. The open-source application, named Electrochemical Reactions in MIcrostructural NEtworks (ERMINE), is implemented within the MOOSE computational framework, and solves species transport coupled to both three-phase boundary and two-phase boundary electrochemical reactions. As the core component, this application is further incorporated into a high-throughput computational workflow. The main advantages of the workflow include:

- Straightforward image-based volumetric meshing that conforms to complex, multi-phased microstructural features
- Computation of local electrochemical fields in morphology-resolved microstructures at considerable length scales

* Corresponding author at: Department of Materials Science and Engineering, Carnegie Mellon University, 5000 Forbes Avenue, Pittsburgh, PA 15213, USA.

E-mail addresses: timhsu@cmu.edu (T. Hsu), rmahbub@andrew.cmu.edu (R. Mahbub), jerry.mason@netl.doe.gov (J.H. Mason), william.epting@netl.doe.gov (W.K. Epting), harry.abernathy@netl.doe.gov (H.W. Abernathy), gregory.hackett@netl.doe.gov (G.A. Hackett), rollett@cmu.edu (A.D. Rollett), litster@andrew.cmu.edu (S. Litster), paulsalvador@cmu.edu (P.A. Salvador).

https://doi.org/10.1016/j.mex.2020.100822

- Implementation on high performance computing platforms, leading to fast, high-throughput computations

ARTICLE INFO
Method name: ERMINE (Electrochemical Reactions in MIcrostructural NEtworks), a MOOSE-based application
Keywords: Fuel cells, Electrodes, Microstructures, Finite element, High performance computation
Article history: Received 27 September 2019; Accepted 24 January 2020; Available online 20 February 2020

Specification Table

Subject Area	Energy
More specific subject area:	Electrochemical modeling of solid oxide fuel cell electrode microstructures
Method name:	ERMINE (Electrochemical Reactions in MIcrostructural NEtworks), a MOOSE-based application
Name and reference of original method	*"Towards Quantification of Local Electrochemical Parameters in Microstructures of Solid Oxide Fuel Cell Electrodes using High Performance Computations,"* ECS Transactions, 78 (1) 2711–2722 (2017) doi: 10.1149/07801.2711ecst
Resource availability	https://edx.netl.doe.gov/dataset/sofc-microstructures-hsu-epting-mahbub-jps-2018 https://github.com/tim-hsu/mink https://www.synopsys.com/simpleware.html https://github.com/tim-hsu/scanip-scripts. http://mooseframework.org/ https://github.com/tim-hsu/ermine

Method Details

Introduction

We present here a computational workflow with an emphasis on the development of a microstructure-based electrochemical simulation framework suitable for high performance computing (HPC) resources. The key steps of the workflow are to acquire, process, mesh, and simulate solid oxide fuel cell (SOFC) cathode microstructures in a high-throughput fashion. The advantages of the workflow, as will be discussed, are:

- High-resolution, large-scale microstructure acquisition
- Straightforward image-based volumetric meshing that conforms to complex, multi-phased microstructures
- Computation of local electrochemical fields in morphology-resolved microstructures at considerable length scales
- Modular nature of user-defined physics; addition or modification of physics requires minimal programming effort
- Implementation on HPC platforms, leading to fast, high-throughput computations

The overall workflow is an extension of the methods detailed in [1–3]. In [2,3], the methods to acquire large volumes of experimental microstructures were described, providing the input experimental microstructures to the numerical modeling approach. In [3], the methods to generate large volume synthetic microstructures were also described. In [1], a reaction-and-transport numerical model was established for solving electrochemical fields inside three-phase cathode microstructures, focusing on the plausibility of computing the oxygen reduction reaction (ORR) at triple phase boundaries (TPBs) along with species transport through the three-phase microstructure of an SOFC cathode. The three phases are the gas conducting phase, or GCP, the electron conducting phase, or ECP (which may also be a mixed ion and electron conducting phase, or MIEP), and the ion conduction phase, or ICP. The initial instantiation of the model, described in [1], only treated the interconnected TPBs as (volumetric) electrochemical reaction sites (for the oxygen reduction reaction, or ORR). In

the updated implementation presented herein, the TPBs are treated similar to before [1], with slight modifications described below, while the ECP is treated as an MIEP, such that the surfaces of the ECP (MIEP) are also considered as active sites for the ORR. All of the physics involved will be documented comprehensively in subsequent sections.

Note that the presented workflow is rather lengthy and involves the usage of several tools, software packages, and programming languages. Therefore, the methods are described both generally, as well as with relevant details to reproduce the work. Throughout the manuscript, links will be provided to data sets and source codes, which are available publicly on open-source sites, including GitHub repositories.

WorkFlow (WF) overview

The overall workflow consists of the following general sequential steps:

1. Segmented Microstructure Acquisition
2. TPB Phase Labeling
3. Pre-Mesh Processing
4. Volumetric Meshing
5. HPC Simulation

Fig. 1 presents a flowchart for the workflow. Each step may be broken down into multiple sub-steps, and their details will be described in later sections, or referenced in the case that the methods were already sufficiently detailed elsewhere. The last step of the workflow, or the simulation step, will be emphasized and separately detailed in a comprehensive manner.

Segmented microstructure acquisition

The first step of the workflow is to acquire three-dimensional (3D) microstructures of interest in the form of segmented 3D image consisted of voxels. The microstructures can be either experimentally captured or synthetically generated. The methods to reconstruct or to generate the microstructures are well documented in [2,3]. Here we briefly summarize these methods.

For experimental microstructures, a Xe-plasma focused ion beam (PFIB) coupled with scanning electron microscope (SEM) was used to perform serial sectioning tomography on SOFC samples [2,3]. The result is a series of two-dimensional SEM micrographs that can be later combined and reconstructed into a three-dimensional (3D) microstructure. The commercial 3D acquisition software “Auto Slice and View” (FEI Company, Hillsboro, OR) was used to automatically perform serial sectioning. After serial-sectioning, the raw stack of SEM images were imported to the software Avizo (FEI version 9.1.1) for post-processing, which involves cropping, aligning, filtering, and segmentation of the images.

For synthetic microstructures, the open-source software DREAM.3D (BlueQuartz Software, Springboro, OH) was used. Users can specify the number of phases, the volume fraction of each phase, and the targeted log-normal distribution of the grain sizes of each phase. Details regarding the construction algorithm are described in [4]. It should be noted that the algorithms are statistical and the targeted (input) grain size is not always obtained in the synthetic microstructure (output) [4].

The scale of acquired microstructures can be substantial, with small voxels on the order of 50–100 nm (edge length) spanning across a (lateral) domain of 150–200 μm. Processing an entire microstructure data at once can be time-consuming or, often, intractable. Therefore, microstructures are usually sub-divided into multiple sub-volumes for further work.

Both the experimental and synthetic microstructures from our work [3] are available at: https://edx.netl.doe.gov/dataset/sofc-microstructures-hsu-epting-mahbub-jps-2018.

Pre-mesh processing

The purpose of pre-mesh processing is to condition the microstructures for later numerical modeling. These processes were implemented using in-house MATLAB scripts, which are available at https://github.com/tim-hsu/mink. The processes are listed below:

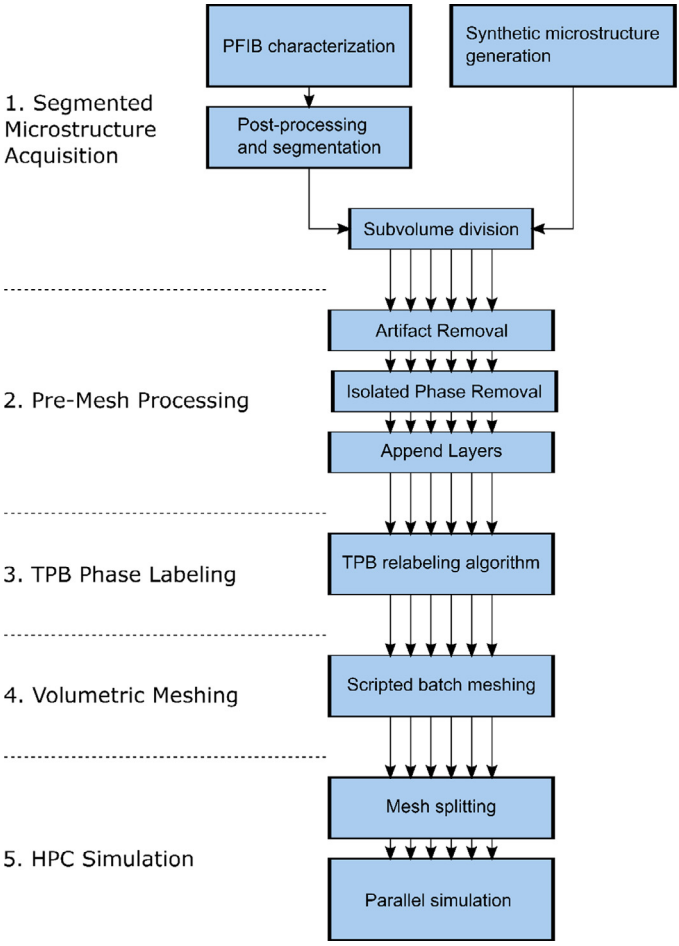

Fig. 1. General flowchart of the computational workflow (except the PFIB characterization, which is an experimental method). Use of multiple arrows in parallel represent the flow of multiple subvolumes of microstructures data processed in parallel.

- Artifact Removal: Sequential Dilation of Phases
- Isolated Phase Removal: Relabel Voxels
- Append Layers: Attach Electrolyte to Bottom[1]

Artifact Removal refers to the process of removing very small isolated features (phases) that are one-to-two voxels wide. These may be artifacts in the experimental data sets from imaging/processing, or outlier small grains in the synthetic data sets. These features should not impact performance but complicate the numerical stiffness. *Sequential dilation* refers to a series of morphological dilation operations that expand phases in a specific order using a structuring element. Similar to morphological opening and closing, it has the effect of removing very small isolated phases with sizes on the order of the structuring element. Details regarding the effect of sequential dilation was also described in [5]. The sequential dilation was typically carried out using a spherical structuring element with a two-voxel radius.

[1] The *bottom {top}* of the microstructure refers to the electrolyte {cathode} side of the domain.

Isolated Phase Removal refers to the process of relabeling isolated phases, or those phases that are not connected (defined by nearest-neighbor connectivity) to the simulation boundaries. These isolated phases arise either by real isolation or by dividing the microstructure to a finite volume. In the current instantiation of ERMINE, these isolated phases cause non-physical solutions. Thus, a voxel labeled as GCP or ECP that has no connection to the top plane[2] of the cathode is re-labeled as an inert phase that has no involvement in the SOFC electrochemistry. Similarly, an ICP voxel that has no connection to the bottom plane[3] of the cathode is re-labeled as an inert phase. Relabeling the isolated phases also results in removal of isolated TPB lineal features (often called inactive TPBs).

Append Layers refers to the process of appending other cell components, such as an electrolyte, an anode, current collectors, etc. The current instantiation of ERMINE is coded for species transport in all layers, but only the ORR electrochemistry in the cathode; it considers the cathode, an electrolyte layer, and an ideal counter electrode as the entire computational domain (discussed later). Thus, a thin electrolyte layer was appended to the bottom of the cathode by simply attaching artificial voxels all labeled as the ICP. In the absence of the thin electrolyte layer, the physics have sharp values at the domain boundary. The appended electrolyte helps smooth the boundary values and represents the physical SOFC better.

TPB phase labeling

In three-phase electrodes, the TPBs are active reaction sites, which generate or deplete relevant electrochemical species. TPBs are considered as one-dimensional (1D) entities in 3D space. There are a few computational approaches to treating the reaction at TPBs [6,7]. In ERMINE, the ORR at TPBs is treated as volumetric source/sink term. To convert the lineal TPBs into volumetric TPBs, the three-phase microstructures are modified such that the voxels located at the intersection of three phases are relabeled as a distinct fourth active phase, or the TPB phase. Details regarding the relabeling algorithm were described in [1]. A 5 $\times$ 5 µm 2D slice of an experimental microstructure is shown in Fig. 2a, containing the four active phases, as described in the caption. Note that the TPB width depends on the resolution (voxel size) of the microstructure. Typically, the volume of TPB voxels is between 0.5% and 4% of the total volume in our microstructure data.

Volumetric meshing

At this point, the microstructure consists of two layers, four active phases (ICP, ECP, GCP, TPB) and an inert phase (the originally isolated phases). To carry out finite element (FE) simulations, which ERMINE uses, the microstructure needs to be meshed. This can be carried out using a variety of meshing methods [7–9], and meshing is often one of the more challenging, time-consuming steps. In our workflow, we used the commercial meshing software Simpleware ScanIP with the FE module (Synopsis, Mountain View, CA). Simpleware ScanIP generates tetrahedral, unstructured meshes in both layers for the four active phases, and maintains mesh connectivity across phases. The commercial software's proprietary algorithm [10] directly operates on voxelated images and, thus, does not require a surface mesh beforehand. Fig. 2b shows how the morphologies are well preserved after meshing the original microstructure (see also [1]), involving almost no user interaction.

ScanIP allows scripting API for interfacing with the software codes and, thus, an automatic meshing workflow was implemented. A user may submit multiple sub-volumes of microstructure data for batch meshing, each with customized parameters. Each meshing procedure is a parallel process using multiple CPU cores. In our case, the software is installed on a workstation with 32 cores, which has been tested to run up to five batch meshing sessions simultaneously. Typically, the meshing runtimes are about 10, 20, 40, and 60–120 min for cubic microstructure volumes with edge lengths of 5, 7.5, 10, and 12.5 µm, respectively. However, the runtime may vary significantly depending on the specifics of each microstructure morphology. Typical meshing times for the two-layer

[2] Oxygen gas and electrons enter the cathode at the top, respectively via the GCP and the ECP.

[3] Oxide ions exit the cathode via the ICP at the bottom of the electrode.

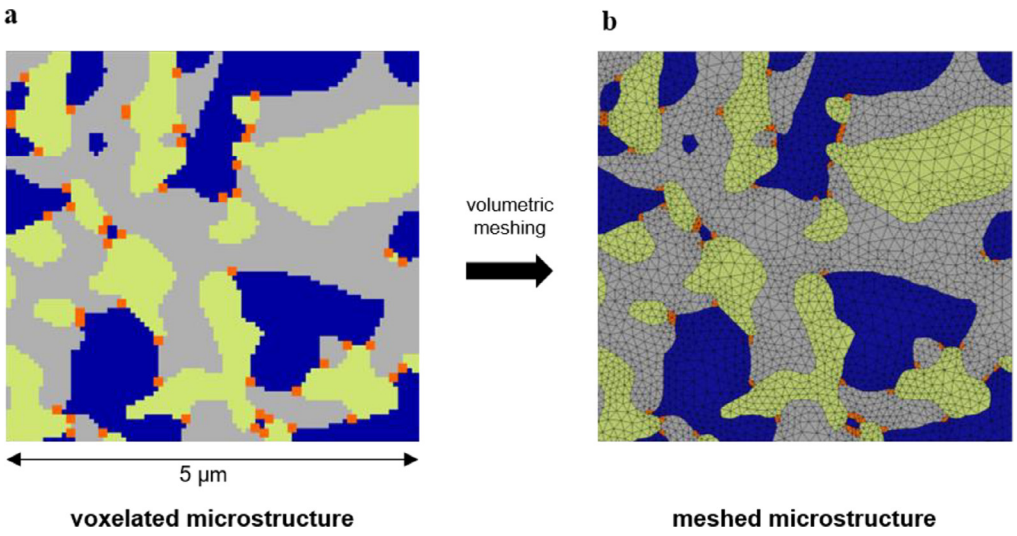

Fig. 2. Visualization of Simpleware ScanIP meshing. A PFIB-characterized microstructure is shown (a) before and (b) after the meshing algorithm (rendered in 2D slice view). The surfaces are well preserved after the meshing. Color indicates phase contrast. The gray phase is pores, the blue phase is lanthanum strontium manganite (LSM), the green phase is yttria-stabilized zirconia (YSZ), the orange phase is the TPBs (For interpretation of the references to color in this figure legend, the reader is referred to the web version of this article.).

$10 \times 10 \times 10$ μm^3 microstructures were 30–45 min. The scripts (written in Python) for batch meshing, along with the meshing parameters, are available at https://github.com/tim-hsu/scanip-scripts.

Fig. 3 visualizes an example of an actual computational domain of an individual subvolume, from a commercial cell cathode. The cathode size is approximately $10 \times 10 \times 7$ μm^3, to which a $10 \times 10 \times 3$ μm^3 electrolyte was appended. Note that the mean particle size of the cathode is 0.46 μm. The phases shown are pores (gray), LSM (blue), YSZ (green), and the TPBs (orange) (which are the GCP, ECP, ICP, and TPB, respectively). Isolated phases are transparent (readily observed as craters on the edges). Fig. 3a highlights the whole domain, without mesh elements: note that the meshed TPBs are difficult to discern owing to their size. Fig. 3b shows only the TPB phase, throughout the whole volume. Fig. 3c highlights the mesh elements near the top front corner of the cathode (as shown in Fig. 3a), where the TPBs are also more readily seen. Fig. 3d highlights how the TPBs are distributed on the ICP in 3D.

HPC simulation

Model formulation

The foundation of the numerical model in this work was established and detailed in [1], which, briefly summarized, is a reaction-and-transport model built for SOFC electrode microstructural meshes in potentiostatic operation. The model receives a predefined reversible half-cell voltage (E_{model}) and a range of global overpotential values (η_{model}) to compute states of local electrochemical quantities (local overpotentials, local current densities, etc.). E_{model} is determined by the oxygen partial pressures at the two sides of the half-cell domain ($p_{O_2,C}$ and $p_{O_2,CE}$), which are located at the top of the cathode and at the bottom of the electrolyte (counter electrode). Fig. 4 illustrates the macroscopic perspective of the model when applied to the computational domain, or the input mesh. j_{model} denotes the global (effective) current density output from the model at a given η_{model}. j_{model} is measured as the average current density flux through the counter electrode.

Previously in [1], the model simulated ORR via the TPB reaction pathway. A second ORR pathway, the MIEC pathway (often called the 2 PB pathway), has since been added. The MIEC pathway accounts for the surface exchange (SE) reaction at the pore/LSM interface and the charge transfer (CT) reaction

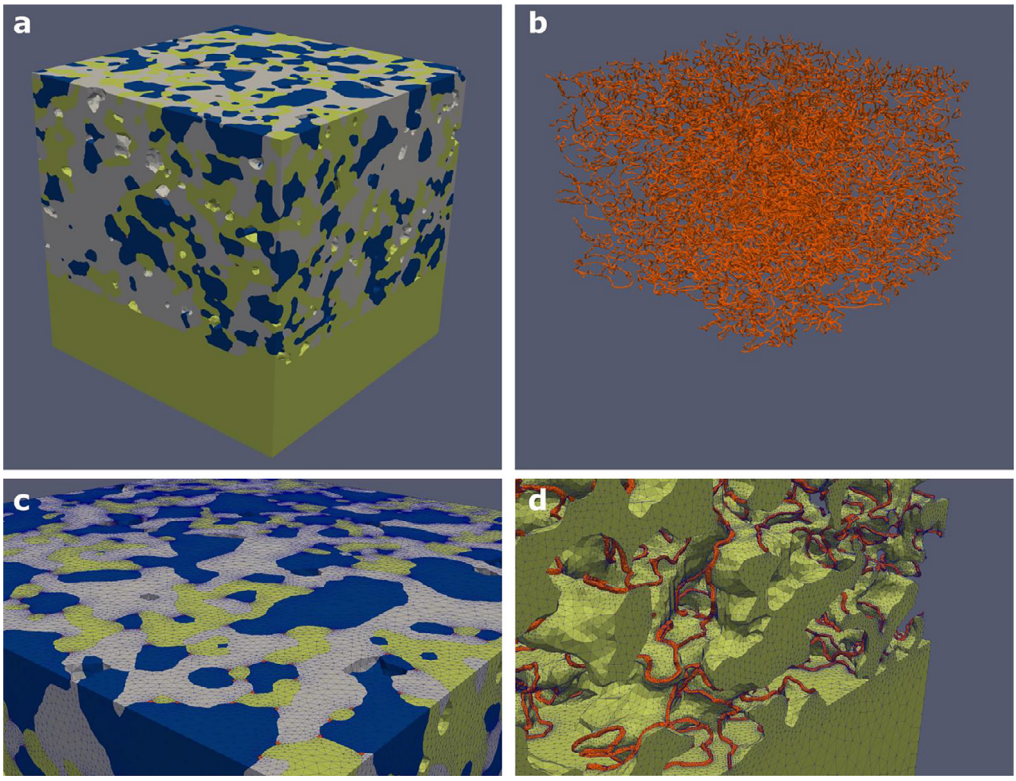

Fig. 3. Rendered images of the unstructured tetrahedral mesh based microstructures derived from a subvolume of a commercial cell cathode from PFIB serial sectioning. (a) All four phases are visualized in this edge rendered image, without mesh elements. The phases shown are pores (gray), LSM (blue), YSZ (green), and the TPBs (orange). Isolated phases are transparent (readily observed as craters on the edges). (b) TPB phase visualized as a surface rendered image. A magnified region of (a) is shown in (c), with the mesh elements rendered. (d) A magnified surface and edge rendered image highlighting the TPB mesh on the YSZ mesh. In this particular subvolume, the numbers of tetrahedral elements for the pore, LSM, YSZ, and TPB phases are respectively ≈ 10.8, 8.9, 6.4, and 3.3 million, which are typical numbers for the subvolume scale in the figure (For interpretation of the references to color in this figure legend, the reader is referred to the web version of this article.).

at the LSM/YSZ interface. In the surface exchange reaction, oxygen gas is reduced and incorporated into LSM as oxide ions reaction at the pore/LSM interface, written as

$$O_{2(g),pore} + 2V_{O,LSM}^{\cdot\cdot} + 4e_{vb,LSM}^{x} \rightarrow 2O_{O,LSM}^{x} + 4h_{vb,LSM}^{\cdot}, \quad (1)$$

in (a modified) Kröger–Vink notation. The MIEC pathway is completed when oxide ions in LSM are then transferred into YSZ via the charge transfer reaction occurring at the LSM/YSZ interface:

$$V_{O,YSZ}^{\cdot\cdot} + O_{O,LSM}^{x} \rightarrow V_{O,LSM}^{\cdot\cdot} + O_{O,YSZ}^{x}. \quad (2)$$

Both interfacial reactions are modeled as reaction fluxes across the interfaces, coupling the separate bulk transport flux in each phase, which will be described later.

Fig. 5 is a visual representation of the ORR pathways in a three-phase cathode composition. Note that only the oxygen species are shown. In LSM, equivalent to oxide ion transport, oxide vacancy transport is modeled instead (described later).

Bulk transports

For all the reactions involved in the ORR pathways, the reaction kinetics depend on bulk transport of reactants to the reaction sites. Gas diffusion, vacancy diffusion, and oxide ionic drift take place in

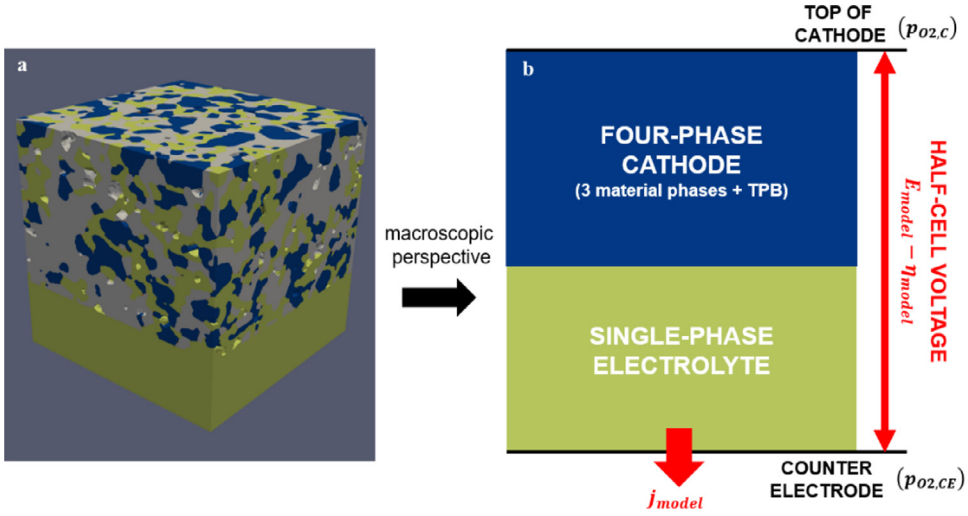

Fig. 4. Schematic of the global parameters of the numerical model with respect to the computational domain geometry. (a) represents the actual mesh domain with microscopic details. This subvolume is the same as that shown in Fig. 3. (b) shows the global parameters in the macroscopic perspective.

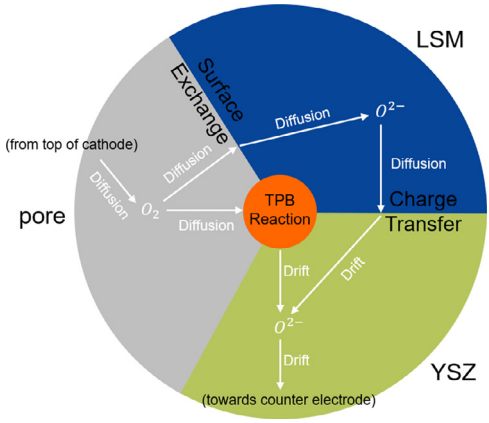

Fig. 5. Schematic of the ORR pathways in three-phase composition. Arrows indicate general directions of oxygen fluxes.

pores, LSM, and YSZ, respectively. Additionally, all bulk transports are defined in the TPB phase as to allow species transport in and out of the TPBs. The mathematical description of oxygen gas diffusion in pores has been slightly modified since the previous work [1]. The model now expresses the oxygen gas diffusion flux as

$$J_{O_2,pore} = -\frac{D_{O_2}}{RT}\nabla p_{O_2}, \tag{3}$$

where D_{O_2} is the oxygen gas diffusivity, R is the gas constant, T is the temperature, and p_{O_2} is the oxygen gas partial pressure. p_{O_2} is a field variable in pores and the TPB phase to be solved numerically. D_{O_2} is a combined diffusivity from the molecular binary diffusivity, D_{ij}, and Knudsen diffusivity, D_{iK}:

$$\frac{1}{D_{O_2}} = \frac{1}{D_{ij}} + \frac{1}{D_{iK}}. \tag{4}$$

Based on the Chapman-Enskog theory, the binary diffusivity of oxygen in nitrogen is estimated as [11]

$$D_{ij} = \frac{0.0018583\ T^{\frac{3}{2}}}{P_{total}\sigma_{ij}\Omega}\left(\frac{1}{M_i}+\frac{1}{M_i}\right)^{\frac{1}{2}}, \tag{5}$$

where P_{total} is the total pressure, σ_{ij} is the collision diameter of the two species, Ω is the dimensionless collision integral based on the interaction of the two species, and M is the molecular weight. The Knudsen diffusivity is estimated as [12]

$$D_{iK} = 4580 d_p\left(\frac{T}{M_i}\right)^{\frac{1}{2}}, \tag{6}$$

where d_p is the mean pore diameter.

In LSM, the oxide ion transport flux may also be described by Fickian diffusion,

$$J_{O,LSM} = -D_{O,LSM}\nabla c_{O,LSM}, \tag{7}$$

where $D_{O,\ LSM}$ is the oxide ion diffusivity of LSM, and $c_{O,\ LSM}$ is the oxide ion concentration in LSM. For the model, $c_{O,\ LSM}$ is expressed in terms of oxide vacancy site fraction in LSM, $[V_O^{\cdot\cdot}]_{LSM}$, as shown in

$$c_{o,LSM} = \frac{3-\left[V_O^{\cdot\cdot}\right]_{LSM}}{a^3 N_A}. \tag{8}$$

Here we assume the LSM crystal structure is cubic with a lattice constant of a, and there is one formula unit per unit cell. N_A is Avogradro's number. The oxide ion diffusion flux can then be rewritten as

$$J_{O,LSM} = -\frac{D_{O,L}}{a^3 N_A}\nabla\left[V_O^{\cdot\cdot}\right]_{LSM}. \tag{9}$$

$[V_O^{\cdot\cdot}]$ is a field variable in LSM and the TPB phase to be solved numerically.

In YSZ, the oxide ionic current flux is described as

$$j_{i,YSZ} = -\sigma_{YSZ}\nabla\phi_{YSZ}, \tag{10}$$

where σ_Y is the oxide ionic conductivity, and ϕ_Y is the YSZ potential, a field variable in YSZ and the TPB phase to be solved numerically. This description is the same as that of the previous work [1].

Reaction rates

Details of the MIEC pathway are described here. The surface exchange rate may be expressed as

$$J_{SE} = -k_{SE}\left(c_{O,eq} - c_{O,LSM}\right), \tag{11}$$

where k_{se} is the exchange coefficient, and $c_{O,\ eq}$ is the equilibrium oxide ion concentration in LSM. For the model, the above equation is expressed in terms of oxide vacancy site fractions,

$$J_{SE} = \frac{k_{SE}}{a^3 N_A}\left(\left[V_O^{\cdot\cdot}\right]_{LSM} - \left[V_O^{\cdot\cdot}\right]_{pore}\right), \tag{12}$$

where $[V_O^{\cdot\cdot}]_{pore}$ is the effective oxide vacancy site fraction as determined by oxygen gas concentration in pores. We refer to Poulsen's work [13] for determining the value of $[V_O^{\cdot\cdot}]_{pore}$ at a given p_{O_2} in the atmosphere. Poulsen modeled the LSM defect chemistry based on several assumed defect generation mechanisms. Various defect populations were computed as a function of p_{O_2}. Using Fig. 6 of Poulsen's work, A linear function for $[V_O^{\cdot\cdot}]_{pore}$ is roughly estimated in the range of $-15 < \log(p_{O_2}) < 0$ with the naked eye. This function serves to compute $[V_O^{\cdot\cdot}]_{pore}$ at a given p_{O_2}, or vice versa.

For the charge transfer reaction, the reaction rate follows a Butler-Volmer form, as shown in

$$j_{CT} = j_{0,CT}\left\{\exp\left(\frac{\alpha z F}{RT}\eta_{ct}\right) - \exp\left(\frac{-(1-\alpha)zF}{RT}\eta_{ct}\right)\right\}, \tag{13}$$

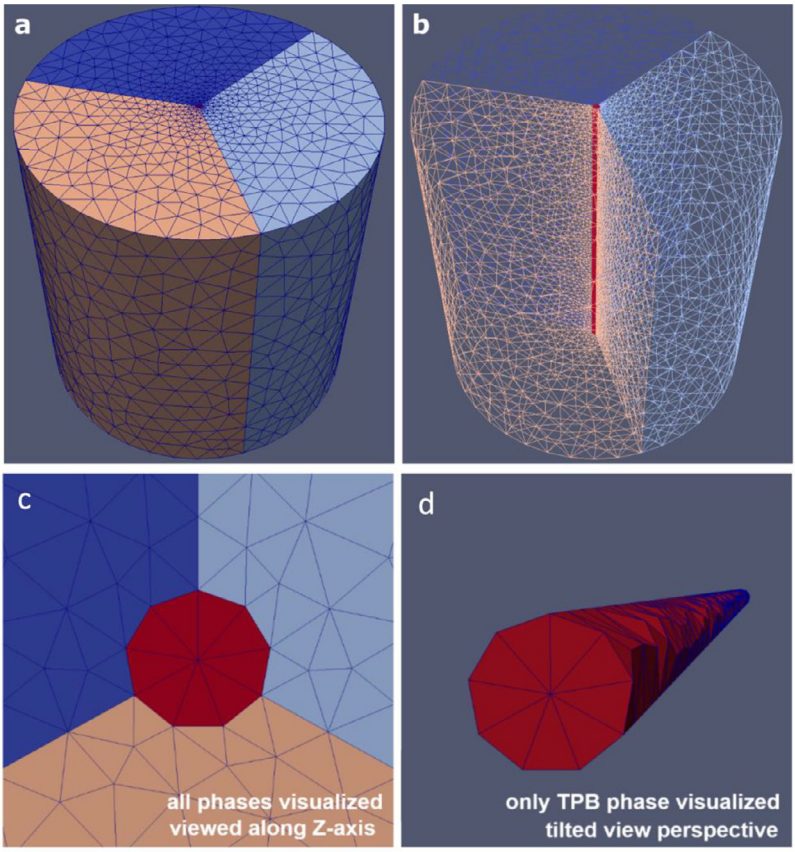

Fig. 6. Visualization of the toy mesh used for testing purposes. This toy mesh has a cylindrical geometry. The mesh is visualized with (a) surface and edge rendering and (b) wireframe rendering. The tetrahedral elements can be seen in (a) and the thin TPB phase elements (in red color) can be seen in (b). The color denotes phase ID. Four colors (phases) are shown in the meshes. Additionally, (c) and (d) visualize the TPB elements in greater detail, with the same rendering mode as (a). The three material phases are transparent in (d).

where $j_{0,\,ct}$ is the exchange current density for the charge transfer reaction, α is the symmetry factor, z is the number of electrons involved in the reaction, the local charge transfer overpotential is

$$\eta_{ct} = E_{ct,rev} - (\phi_{LSM} - \phi_{YSZ}). \tag{14}$$

The definition of ϕ_{LSM} was described in the previous work [1].

The charge transfer reversible potential, $E_{ct,\,rev}$ is determined by

$$E_{CT,rev} = -\frac{RT}{4F} \ln\left(\frac{p_{O_2,CE}}{p_{O_2,LSM}}\right), \tag{15}$$

where $p_{O_2,LSM}$ is the *effective* p_{O_2} in LSM based on the local value of $[V_O^{\cdot\cdot}]_{LSM}$. $p_{O_2,LSM}$ is calculated using the linear function based on Poulsen's work mentioned earlier.

The TPB reaction rate has been modified from the previous work. Its rate follows the Butler-Volmer form,

$$s_{TPB} = s_{0,TPB}\left\{\exp\left(\frac{\alpha z F}{RT}\eta_{TPB}\right) - \exp\left(\frac{-(1-\alpha)zF}{RT}\eta_{TPB}\right)\right\}, \tag{16}$$

where $s_{0,\,TPB}$ is the exchange rate, and the local TPB reaction overpotential is

$$\eta_{TPB} = E_{CT,rev} - (\phi_{LSM} - \phi_{YSZ}). \tag{17}$$

The TPB reaction reversible potential is determined by

$$E_{CT,rev} = -\frac{RT}{4F}\ln\left(\frac{p_{O_2,CE}}{p_{O_2}}\right). \tag{18}$$

Note that the TPB reaction rate here is volumetric [A/cm^3]. The exchange rate, $s_{0,\,TPB}$, can be derived from a measured lineal exchange current density, $j_{0,\,TPB}$ [A/cm]. Miyoshi et al. [14] proposed an empirical formula for $j_{0,\,TPB}$ that specifically targets ORR at the TPB. Thus, the volumetric exchange rate is derived by writing

$$s_{0,TPB}\left[\frac{A}{cm^3}\right] = j_{0,TPB}\left[\frac{A}{cm}\right]\frac{L_{TPB}[cm]}{V_{total}\left[cm^3\right]}\frac{V_{total}\left[cm^3\right]}{V_{TPB}\left[cm^3\right]}, \tag{19}$$

where L_{TPB} is the TPB lineal length, V_{total} is the total volume (of a cathode subvolume), and V_{TPB} is the total volume of the TPB mesh elements in the microstructural mesh.

Model summary

In summary, the expressions for the bulk transport fluxes are

$$\begin{cases} J_{O_2,pore} = -\dfrac{D_{O_2}}{RT}\nabla p_{O_2} \\ J_{O,LSM} = -\dfrac{D_{O,L}}{a^3 N_A}\nabla\left[V_{\ddot{O}}\right]_{LSM} \\ j_{i,YSZ} = -\sigma_{YSZ}\nabla\phi_{YSZ} \end{cases}. \tag{20}$$

The expressions for the local reaction rates are

$$\begin{cases} J_{SE} = \dfrac{k_{SE}}{a^3 N_A}\left(\left[V_{\ddot{O}}\right]_{LSM} - \left[V_{\ddot{O}}\right]_{pore}\right) \\ j_{CT} = j_{0,ct}\left\{\exp\left(\dfrac{\alpha zF}{RT}\eta_{ct}\right) - \exp\left(\dfrac{-(1-\alpha)zF}{RT}\eta_{ct}\right)\right\} \\ s_{TPB} = s_{0,TPB}\left\{\exp\left(\dfrac{\alpha zF}{RT}\eta_{TPB}\right) - \exp\left(\dfrac{-(1-\alpha)zF}{RT}\eta_{TPB}\right)\right\} \end{cases}. \tag{21}$$

The expressions above are combined in the form of continuity equations for mass (and charge) conservation. The local conservation for pore, LSM, and YSZ is written as

$$\begin{cases} \nabla\cdot\left(J_{O_2,pore}\right) = -\dfrac{s_{TPB}}{zF} \\ \nabla\cdot\left(J_{O,LSM}\right) = 0 \\ \nabla\cdot\left(j_{i,YSZ}\right) = -s_{TPB} \end{cases}. \tag{22}$$

It is important to point out that each transport reaction rate is region-specific (phase-specific). For example, oxygen ionic flux in YSZ is not defined in pores and LSM. Thus the term $j_{i,\,YSZ}$ is not defined anywhere but the YSZ phase. Likewise, s_{TPB} is not defined (and hence zero) anywhere outside the TPB mesh elements. Finally, note that J_{SE} acts as a sink for p_{O_2} and $[V_{\ddot{O}}]_{LSM}$. j_{CT} acts as a source for $[V_{\ddot{O}}]_{LSM}$ and a sink for ϕ_{YSZ}. s_{TPB} acts as a sink for p_{O_2} and ϕ_{YSZ}. One has to convert the unit properly (divide by zF) when calculating the reaction rates for each field variable in the corresponding phase.

The typical boundary and initial conditions are listed in Table 1. The initial value of $[V_{\ddot{O}}]_{LSM}$ corresponds to an effective oxygen concentration of 0.21 [atm] and displays many significant digits in order to match 0.21 [atm] as close as possible (a low number of significant digits does not convert to 0.21 [atm] with high precision).

Table 1
Model parameters.

Notation	Description	Value	Unit	Reference
T	Temperature	1073	K	–
η_{model}	Model (global) overpotential	Varies (model input)	V	–
$p_{O_2,c}$	[Boundary Condition] Oxygen partial pressure at top of cathode	0.21	atm	–
$p_{O_2,CE}$	Oxygen partial pressure at counter electrode	1e-20	atm	–
E_{model}	Reversible half-cell potential (or OCV)	1.028	V	–
$\phi_{YSZ,\ CE}$	[Boundary Condition] Potential at counter electrode	0	V	–
D_{O_2}	Oxygen gas diffusivity	0.64	cm^2/s	–
$D_{O,\ LSM}$	Oxygen diffusivity in LSM	7.5e-7	cm^2/s	[16]
σ_{YSZ}	YSZ ionic conductivity	4e-2	S/cm	[17]
k_{SE}	Chemical surface exchange coefficient	6.14e-6	cm/s	[18]
$j_{0,\ CT}$	Charge transfer exchange current density	0.193	A/cm^2	[19]
$j_{0,\ TPB}$	Lineal TPB reaction exchange current density	1e-7	A/cm	[14]
z	Number of electrons for TPB and charge transfer reaction	4	–	–
α	Symmetry factor TPB and charge transfer reaction	0.5	–	–
p_{O_2}	[Initial Condition] Oxygen partial pressure in pores	0.21	atm	–
$[V_O^{\cdot\cdot}]_{LSM}$	[Initial Condition] Oxygen vacancy site fraction in LSM	2.580947226225166e-8	–	–
ϕ_{YSZ}	[Initial Condition] Electric potential in YSZ	0	V	–

The MOOSE framework and ERMINE

As described in the previous work [1], a MOOSE-based application named ERMINE (Electrochemical Reactions in MIcrostructural NEtworks) was developed to implement the model. MOOSE (Idaho National Laboratory, Idaho Falls, ID) is an open-source finite element library designed for massively parallel multiphysics simulations [15]. Further details regarding our implementation of MOOSE and ERMINE can be found in [1], and ERMINE has since been updated to account for the changes described in this work. The ERMINE source codes are available at https://github.com/tim-hsu/ermine.

Mesh splitting and parallel simulation

To the author's knowledge, in general, a normal FE simulation run in MOOSE may be carried out by multiple cores in parallel. However, each core would still hold an amount of memory roughly equal to the memory usage of the mesh (plus the amount for model computation). In this scenario, a 200-core simulation applied to a 1GB mesh may require beyond 200 GB of memory usage. *Mesh splitting* refers to dividing the microstructural mesh into multiple parts and is a way to distribute the memory usage of a mesh to multiple cores such that each core only holds a fraction of the memory of the mesh. This process can be simply implemented by a built-in executable within the MOOSE framework and has been observed to be essential for memory-limited cluster nodes (under 64 GB). We have carried out simulations that theoretically access up to 1.5 TB of node memory, though a more robust benchmark of the actual memory usage has not been done.

We implemented the ERMINE application on laptops and workstations for the testing and debugging stages. Two supercomputers are used for the production stage: Joule (National Energy Technology Laboratory, Morgantown, WV) and Bridges (Pittsburgh Supercomputing Center, Pittsburgh, PA). Typically, for domains of $10 \times 10 \times 10\ \mu m^3$ (exactly the size of the subvolume in Fig. 3 with a mean particle size of 0.46 μm), a suitable number of cores is about 256. So far, increasing the domain size has not led to a substantial increase in simulation runtime (due to the increase in the number of cores used). The typical runtime for a such subvolume may range from ten minutes to 1–2 h, making the high-throughput workflow (simulating tens or hundreds of subvolumes) a reality.

Model (Method) validation

To validate that the physics coded in ERMINE are modeled properly, a toy mesh with simple geometry (similar to Fig. 5) was used for ease of visualization, as shown in Fig. 6. Note that the top {bottom} side is the boundary condition for oxygen gas entrance {oxygen ion exit}.

Simulation of ORR based on this simple mesh—with the TPB and the MIEC pathways separately simulated—is shown in Fig. 7. Note that only the YSZ phase is visualized. The arrows indicate local

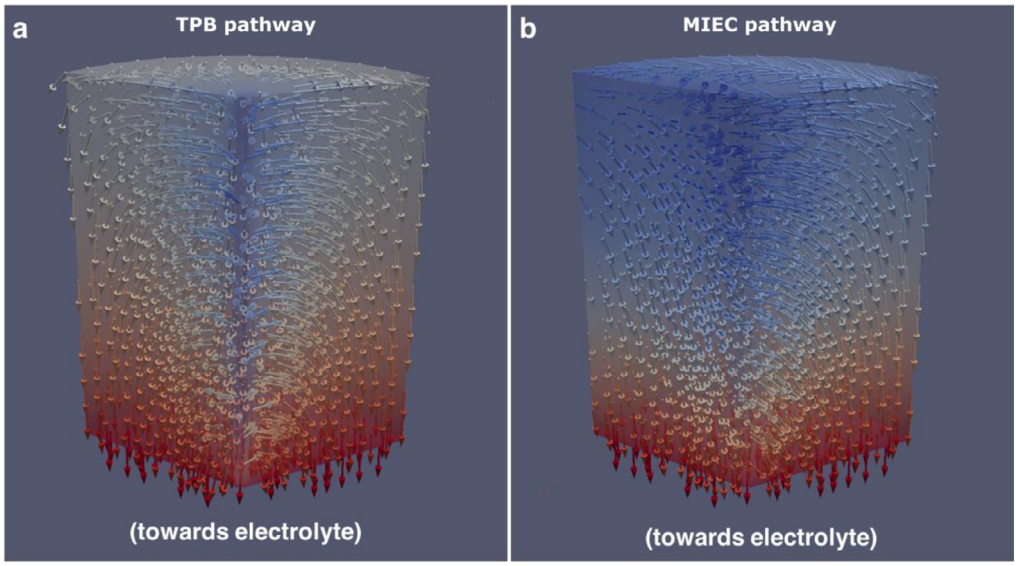

Fig. 7. Visualization of oxygen ion flux based on the simple toy mesh. Color indicates the YSZ potential (V) distribution at a given global overpotential (blue is low potential, $\approx -1.4 \times 10^{-2}$ in (a) and $\approx -1.5 \times 10^{-7}$ in (b), and red is high potential, $\approx$ 0 V). Only the YSZ phase is shown with a degree of transparency. The potential gradient vectors, or effectively, the oxygen ionic flux vectors, are represented by the arrows. Two scenarios from the axial TPB model are presented, which are (a) the TPB and (b) the MIEC pathways. The arrows only represent flux directions, not magnitude (they are not to scale) (For interpretation of the references to color in this figure legend, the reader is referred to the web version of this article.).

Table 2
Relative contributions of TPB, MIEC, and combined pathways.

η_{model} [V]	j (TPB) [A/cm^{-2}]	j (MIEC) [A/cm^{-2}]	j (TPB + MIEC) [A/cm^{-2}]
0.004	0.005647	1.87e-08	0.005644
0.0116	0.015393	3.31e-08	0.015379
0.02604	0.034898	4.62e-08	0.034886
0.04	0.056031	9.70e-08	0.056021
0.08	0.140035	5.55e-07	0.139874
0.12	0.282308	2.34e-06	0.282139
0.16	0.516044	5.42e-06	0.515975
0.2	0.883689	1.25e-05	0.883673
0.24	1.443451	2.71e-05	1.443491
0.288	2.471906	7.26e-05	2.472064
0.3456	4.38199	3.39e-05	4.382305
0.4	6.952363	4.92e-04	6.952993

ionic flux directions in the YSZ phase. In (a), oxygen ions generated at the TPBs flow away from the TPBs and downward to the electrolyte. In (b), oxygen ions generated at the LSM/YSZ interface flow away from the interface and downward to the electrolyte. Fig. 7 illustrates that ERMINE is properly modeling the local reactions and transport, as expected from the concept shown in Fig. 5.

The relative contributions of the TPB and the MIEC pathways based on a real microstructure (same as that in Fig. 4) are quantified below. Three scenarios were simulated using the parameters listed in Table 1: only the TPB pathway, only the MIEC pathway, and both pathways. The effective current density (j)—which is the mean current density exiting the electrolyte layer—was measured across a range of model/global overpotentials (η_{model}), as shown in Table 2.

Based on the current parameter setting, the MIEC pathway has negligible contribution to the effective performance. This would make sense since LSM is not known to be an excellent MIEC.

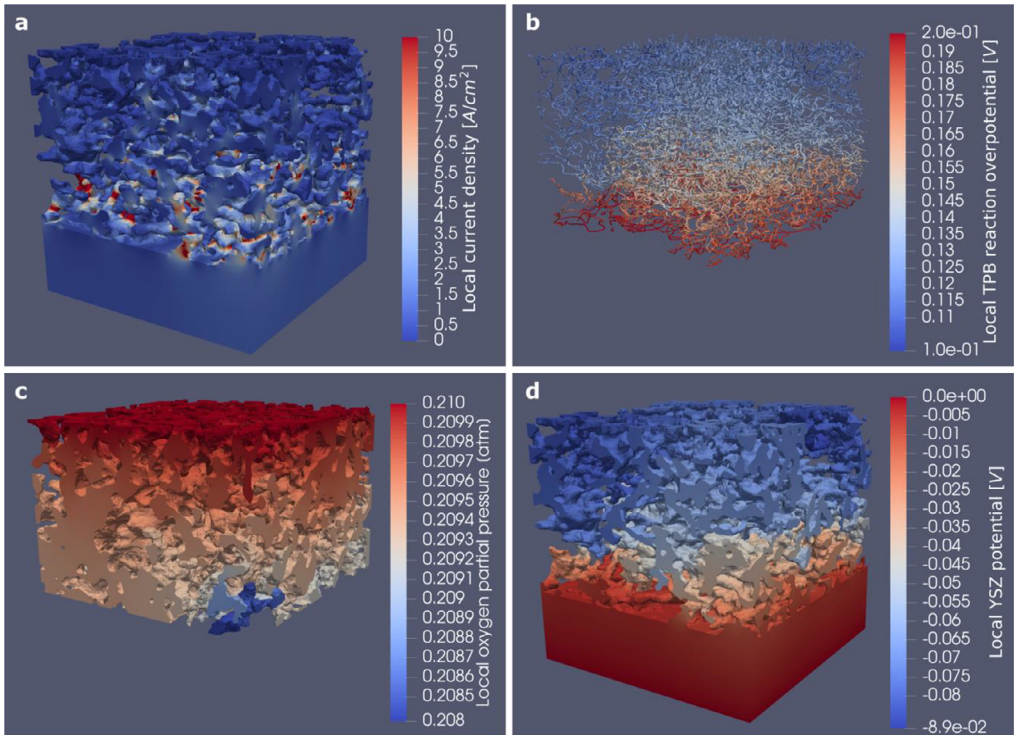

Fig. 8. Simulation output as evaluated at the mesh element nodes, rendered in Paraview. The individual mesh elements are not visible here due to the rendering mode. (a) $j_{i,\ YSZ}$ in YSZ. (b) η_{TPB} in the TPB phase. (c) p_{O_2} in pores. (d) ϕ_{YSZ} in YSZ. Color indicates magnitude of the shown quantities.

However, for future work, we may investigate cases when the MIEC pathway (or both TPB and MIEC) is dominant by adjusting the model parameters. The same can be done when investigating different materials that relate to different rate coefficients.

Fig. 8 shows several different aspects of the simulation output based on the microstructure subvolume shown in Fig. 4. The simulation was run on Joule using 256 cores, with the model parameters and the boundary conditions listed in Table 1. The runtime was about 30 min. The output consists of fields of local variables (p_{O_2}, $[V_{\ddot{O}}]_{LSM}$, and ϕ_{YSZ}) that are discretized and evaluated at the nodes of the microstructure mesh elements. Fig. 8a,b,c,d show $j_{i,\ YSZ}$ in YSZ, η_{TPB} in the TPB phase, p_{O_2} in pores, and ϕ_{YSZ} in YSZ, respectively. Quantities such as p_{O_2} and ϕ_{YSZ} were directly solved during the simulation, while $j_{i,\ YSZ}$ and η_{TPB} were computed during post-processing using Paraview (Kitware Inc., Clifton Park, NY & Sandia National Laboratories, Albuquerque, NM).

Although ERMINE computes fields of local electrochemical quantities, *effective* performance metrics can be quantified. Specifically, we calculated the current density flux through the bottom plane of the electrolyte layer of the simulation output shown in Fig. 8. This quantity, j_{model}, varies with the model overpotential, η_{model}. Therefore we can plot (as done in Fig. 9) the *effective* performance (current output vs. applied overpotential) of the cathode microstructure.

To validate our model, we compare the simulation output with two effective medium theory models in the literature – the TFV model [20,21], and the DREAM SOFC model [22,23]. We use a specific variant of the TFV model and the parameters as described in [21]. The parameters used for the DREAM SOFC model are the same as listed in Table 1. These two effective medium theory models were implemented with the same subvolume of the microstructure shown in Fig. 4. The effective performances from the three models are shown in Fig. 9. η_c is the model overpotential applied

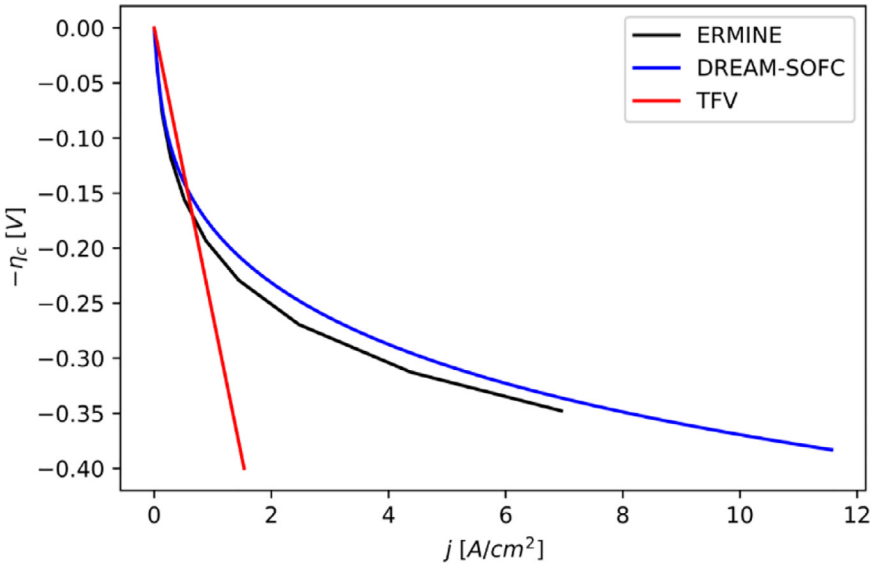

Fig. 9. Effective performance outputs from ERMINE, DREAM SOFC, and TFV models. η_c denotes the model overpotential applied across the cathode layer, and j is the current density output.

across the cathode layer, and j is the effective current density output. These models are in reasonable agreement, however some discrepancies exist. These discrepancies are described extensively in a companion paper [25], which derives conclusions from the ability of ERMINE to be run in a high-throughput fashion on HPC platforms, and which generates a statistical view of microstructure-performance parameters.

Basic scaling test

A basic scaling test was performed to validate the necessity of high performance computing resources and the scaling capacity of ERMINE. A sample microstructure subvolume of the same type as the microstructure shown in Fig. 3 was meshed and used for the test. Its physical size is $10 \times 10 \times 10$ µm^3 (which includes a 3 µm electrolyte thickness), and its number of mesh elements is roughly 25–30 million. The simulations were run on Bridges' regular compute nodes, with the parameters listed in Table 1.

Here we define the runtime T (different from temperature previously defined) of an (parallel) algorithm/process to be the time elapsed between the start of the process and its termination. We also define the speedup of a parallel process to be the ratio of the serial runtime to the parallel runtime:

$$Speedup = \frac{T_s}{T_p}, \tag{23}$$

where T_s is the serial runtime, and T_p is the parallel runtime using p cores. Finally, the efficiency of a parallel process is defined as

$$Efficiency = \frac{T_s}{pT_p}. \tag{24}$$

Efficiency is a measure of how efficiently each core is used during the parallel computation; it ranges from 0 (no useful core utilization) to 1 (perfect per-core efficiency).

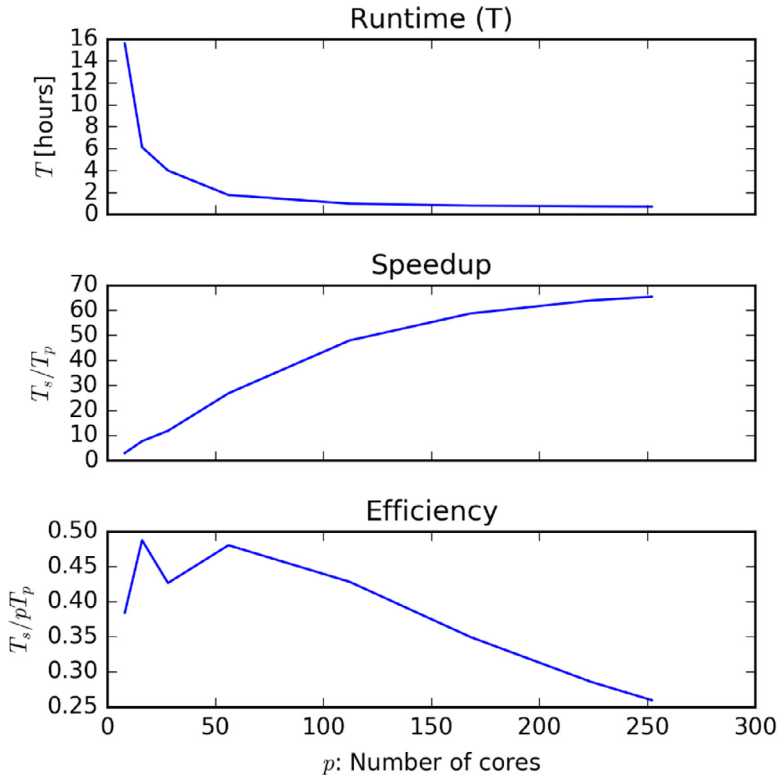

Fig. 10. Runtime, speedup, and efficiency of a sample parallel simulation as a function of number of cores.

Fig. 10 shows the runtime, speedup, and efficiency, each a function of number of cores (p) used, of running ERMINE based on the 10 × 10 × 10 μm^3 microstructure subvolume similar to that of Fig. 3. It is clear that the use of parallel cores can drastically reduce the runtime. In fact, the simulation could not be run serially (i.e., using only one core) or with a small p due to extremely slow computation rate. Even at $p = 4$, the simulation runtime exceeded the maximum allowed wall time on Bridges' regular nodes (48 h), and the simulation was forced to terminate. At high p, the runtime drastically decreases to almost 0 h, suggesting that ERMINE's scaling capacity can accommodate a larger microstructure mesh with roughly $p > 100$. Since a truly serial runtime could not be acquired, we assumed the serial runtime was at least $T_s = 48$ h (the maximum allowed wall time per compute session). Using this lower limit assumption, the speedup can reach almost 70 times the minimum serial speed. Since $T_s > 48$ h, the true speedup values will be larger. Further, the speedup has not quite plateaued yet at $p = 252$, suggesting again that ERMINE's scaling capacity has not been fully strained. Finally, the maximum efficiency is roughly located between $p =$ 10–50, with values between 0.45 and 0.5, though there is a dip in this range to $\approx$ 0.42. Keeping in mind that this is based on an approximated minimal speedup value, the true values will be higher efficiencies. Without further monitoring more factors such as real-time inter-node communication overhead, memory usage, etc., it is difficult to explain the dip. At $p = 252$, the minimal efficiency reaches 0.25, but has not dropped to 0. This suggests that a higher p can still be used before depleting the efficiency.

Overall, Fig. 10 demonstrates that high performance computing resources are essential for conducting ERMINE's non-linear electrochemistry simulations based on complex microstructure domains. Further, this basic test demonstrates that ERMINE's compute performance has not been fully strained on Bridges; the test reveals some promise for ERMINE to incorporate a larger domain size or higher model complexity before depleting core efficiency.

Disclaimer

This work was funded by the Department of Energy, National Energy Technology Laboratory, an agency of the United States Government, through a support contract with Leidos Research Support Team (LRST). Neither the United States Government nor any agency thereof, nor any of their employees, nor LRTS, nor any of their employees, makes any warranty, expressed or implied, or assumes any legal liability or responsibility for the accuracy, completeness, or usefulness of any information, apparatus, product, or process disclosed, or represents that its use would not infringe privately owned rights. Reference herein to any specific commercial product, process, or service by trade name, trademark, manufacturer, or otherwise, does not necessarily constitute or imply its endorsement, recommendation, or favoring by the United States Government or any agency thereof. The views and opinions of authors expressed herein do not necessarily state or reflect those of the United States Government or any agency thereof.

Acknowledgments

This work was performed in support of the National Energy Technology Laboratory's ongoing research in solid oxide fuel cells under the RSS contract 89243318CFE000003. This project was supported in part by an appointment to the Internship/Research Participation Program at the National Energy Technology Laboratory, U.S. Department of Energy, administered by the Oak Ridge Institute for Science and Education. The authors acknowledge the use of the computing workstation at Materials Characterization Facility at Carnegie Mellon University supported by grant MCF-677785. This work was also supported in part by a CMU ProSEED/EQT Foundation Grant.

This work used the Joule supercomputer at the National Energy Technology Laboratory, and the Bridges system [24], which is supported by NSF award number ACI-1445606, at the Pittsburgh Supercomputing Center (PSC). We thank the MOOSE user community and the MOOSE developers at the Idaho National Laboratory for general guidance on the MOOSE framework.

Declaration of Competing Interest

The Authors confirm that there are no conflicts of interest.

References

[1] T. Hsu, R. Mahbub, W.K. Epting, H. Abernathy, G.A. Hackett, A.D. Rollett, S. Litster, P.A. Salvador, Towards quantification of local electrochemical parameters in microstructures of solid oxide fuel cell electrodes using high performance computations, ECS Trans. 78 (2017) 2711–2722, doi:10.1149/07801.2711ecst.

[2] R. Mahbub, T. Hsu, W.K. Epting, N.T. Nuhfer, G.A. Hackett, H. Abernathy, A.D. Rollett, M. De Graef, S. Litster, P.A. Salvador, A method for quantitative 3D mesoscale analysis of solid oxide fuel cell microstructures using xe-plasma focused ion beam (PFIB) coupled with SEM, ECS Trans. 78 (2017) 2159–2170, doi:10.1149/07801.2159ecst.

[3] T. Hsu, W.K. Epting, R. Mahbub, N.T. Nuhfer, S. Bhattacharya, Y. Lei, H.M. Miller, P.R. Ohodnicki, K.R. Gerdes, H.W. Abernathy, G.A. Hackett, A.D. Rollett, M. De Graef, S. Litster, P.A. Salvador, Mesoscale characterization of local property distributions in heterogeneous electrodes, J. Power Sources 386 (2018) 1–9, doi:10.1016/j.jpowsour.2018.03.025.

[4] M. Groeber, S. Ghosh, M.D. Uchic, D.M. Dimiduk, A framework for automated analysis and simulation of 3D polycrystalline microstructures. part 2: synthetic structure generation, Acta Mater 56 (2008) 1274–1287, doi:10.1016/j.actamat.2007.11.040.

[5] W.K. Epting, Z. Mansley, D.B. Menasche, P. Kenesei, R.M. Suter, K. Gerdes, S. Litster, P.A. Salvador, Quantifying intermediate-frequency heterogeneities of SOFC electrodes using X-ray computed tomography, J. Am. Ceram. Soc. 100 (2017) 2232–2242, doi:10.1111/jace.14775.

[6] K. Matsuzaki, N. Shikazono, N. Kasagi, Three-dimensional numerical analysis of mixed ionic and electronic conducting cathode reconstructed by focused ion beam scanning electron microscope, J. Power Sources 196 (2011) 3073–3082, doi:10.1016/j.jpowsour.2010.11.142.

[7] A. Bertei, V. Yufit, F. Tariq, N.P. Brandon, A novel approach for the quantification of inhomogeneous 3D current distribution in fuel cell electrodes, J. Power Sources 396 (2018) 246–256, doi:10.1016/j.jpowsour.2018.06.029.

[8] M.E. Lynch, D. Ding, W.M. Harris, J.J. Lombardo, G.J. Nelson, W.K.S. Chiu, M. Liu, Flexible multiphysics simulation of porous electrodes: conformal to 3D reconstructed microstructures, Nano Energy 2 (2013) 105–115, doi:10.1016/j.nanoen.2012.08.002.

[9] T. Carraro, J. Joos, B. Rüger, A. Weber, E. Ivers-Tiffée, 3D finite element model for reconstructed mixed-conducting cathodes: I. performance quantification, Electrochim. Acta. 77 (2012) 315–323, doi:10.1016/j.electacta.2012.04.109.

[10] P.G. Young, T.B. Beresford-West, S.R. Coward, B. Notarberardino, B. Walker, A. Abdul-Aziz, An efficient approach to converting three-dimensional image data into highly accurate computational models, Philos. Trans. R. Soc. A Math. Phys. Eng. Sci. 366 (2008) 3155–3173, doi:10.1098/rsta.2008.0090.

[11] E.L. Cussler, Diffusion: mass transfer in fluid systems, Engineering (1997), doi:10.1017/CBO9780511805134.010.
[12] J.R. Welty, C.E. Wicks, R.E. Wilson, G. Rorrer, Fundamentals of Momentum, Heat and Mass Transfer, John Wiley & Sons, 1970, doi:10.1016/0017-9310(70)90063-3.
[13] F.W. Poulsen, Defect chemistry modelling of oxygen-stoichiometry, vacancy concentrations, and conductivity of (La1-xSrx)yMnO3±δ, Solid State Ionics 129 (2000) 145–162, doi:10.1016/S0167-2738(99)00322-7.
[14] K. Miyoshi, T. Miyamae, H. Iwai, M. Saito, M. Kishimoto, H. Yoshida, Exchange current model for (La0.8Sr0.2)0.95MnO3 (LSM) porous cathode for solid oxide fuel cells, J. Power Sources 315 (2016) 63–69, doi:10.1016/j.jpowsour.2016.02.076.
[15] D. Gaston, C. Newman, G. Hansen, D. Lebrun-Grandié, MOOSE: a parallel computational framework for coupled systems of nonlinear equations, Nucl. Eng. Des. 239 (2009) 1768–1778, doi:10.1016/j.nucengdes.2009.05.021.
[16] A. Belzner, T.M. Gür, R.A. Huggins, Oxygen chemical diffusion in strontium doped lanthanum manganites, Solid State Ionics 57 (1992) 327–337, doi:10.1016/0167-2738(92)90166-M.
[17] Y. Ji, J.A. Kilner, M.F. Carolan, Electrical properties and oxygen diffusion in yttria-stabilised zirconia (YSZ)-La0.8Sr0.2MnO3±δ (LSM) composites, Solid State Ionics 176 (2005) 937–943, doi:10.1016/j.ssi.2004.11.019.
[18] L. Yan, B. Kavaipatti, K.-.C. Chang, H. You, P. Salvador, Microstructural effects on the oxygen exchange kinetics of La0.7Sr0.3MnO3 thin films, ECS Trans. (2011), doi:10.1149/1.3570197.
[19] M. Gong, R.S. Gemmen, X. Liu, Modeling of oxygen reduction mechanism for 3PB and 2PB pathways at solid oxide fuel cell cathode from multi-step charge transfer, J. Power Sources 201 (2012) 204–218, doi:10.1016/j.jpowsour.2011.11.002.
[20] C.W. Tanner, The effect of porous composite electrode structure on solid oxide fuel cell performance, J. Electrochem. Soc. 144 (1997) 21, doi:10.1149/1.1837360.
[21] J.S. Cronin, Y.K. Chen-Wiegart, J. Wang, S.a. Barnett, Three-dimensional reconstruction and analysis of an entire solid oxide fuel cell by full-field transmission X-ray microscopy, J. Power Sources 233 (2013) 174–179, doi:10.1016/j.jpowsour.2013.01.060.
[22] J. Mason, I. Celik, S. Lee, H. Abernathy, G. Hackett, Performance degradation predictions based on microstructural evolution due to grain coarsening effects in solid oxide fuel cell electrodes, J. Electrochem. Soc. 165 (2018) F64–F74, doi:10.1149/2.0721802jes.
[23] S.R. Pakalapati, A new reduced order model for solid oxide fuel cells Ph.D. Thesis, West Virginia University Libraries, 2006.
[24] T. Hsu, J.H. Mason, R. Mahbub, W.K. Epting, H.W. Abernathy, G.A. Hackett, A.D. Rollett, S. Litster, P.A. Salvador, Distributions of local electrochemistry in heterogeneous microstructures of solid oxide fuel cells using high-performance computations, Electrochimica Acta Submitted for publication.
[25] N.A. Nystrom, M.J. Levine, R.Z. Roskies, J.R. Scott, Bridges: a uniquely flexible HPC resource for new communities and data analytics, in: Proceedings of the 2015 Annual Conference on Extreme Science and Engineering Discovery Environment (St. Louis, MO, July 26-30, 2015). XSEDE15, ACM, New York, NY, USA, 2015, doi:10.1145/2792745.2792775.